THE k^{-2} RUPTURE MODEL PARAMETRIC STUDY: EXAMPLE OF THE 1999 ATHENS EARTHQUAKE

F. GALLOVIČ*, J. BROKEŠOVÁ

Department of Geophysics, Faculty of Mathematics and Physics, Charles University, V Holešovičkách 2, 180 00 Prague 8, Czech Republic (gallovic@karel.troja.mff.cuni.cz, johana@seis.karlov.mff.cuni.cz)

* Corresponding author

Received: December 20, 2002; Revised: November 10, 2003; Accepted: March 22, 2004

ABSTRACT

We employ a realistic finite-extent "k^{-2}" stochastic source model with k-dependent rise time, introduced by Bernard et al. (1996) and extended by Gallovič and Brokešová (2004), to synthesize the strong ground motions in near source distances. For a given magnitude, this rupture model involves a number of free parameters (fault dimensions, slip roughness, maximum rise time, slip velocity function). We study their influence on the peak ground acceleration (PGA) maps (parametric study) for an example of the 1999 Athens earthquake of $M_w = 5.9$. The observed macroseismic intensities serve us as a rough constraint on the simulated PGA's to find a set of suitable k^{-2} models. These models agree with empirical source scaling relations.

Keywords: finite-extent source modelling, strong ground motion accelerograms, k^{-2} slip distribution, k-dependent rise time, 1999 Athens earthquake

1. INTRODUCTION

The earthquake engineers need realistic estimates of ground motion time series to build seismically resistant structures. While the low frequency records (displacement) can be successfully modelled with the simple assumption of smooth (or even constant) slip and constant rupture velocity (e.g., Haskell model), the high frequency randomness of the wave field (commonly observed in acceleration) requires more complex approaches to be applied.

Bernard and Herrero (1994) and *Herrero and Bernard (1994)* introduced the k^{-2} stochastic source model (k being the wave number) for strong ground motion modelling. This approach belongs in the class of kinematic methods of strong ground motion simulations. It involves a stochastic part in slip distribution.

The k^{-2} approach was used in the strong motion prediction by *Zollo et al. (1997)* and *Emolo and Zollo (2001)*. In these papers it has been shown that the radiated source spectra satisfy commonly observed ω^2 scaling law (*Aki, 1967*). However, only the instantaneous

rise time was considered in these studies. *Bernard et al. (1996)* modified this approach by considering more realistic, boxcar, slip velocity function with *k*-dependent rise time. It has been successfully used for past as well as possible future earthquakes by *Berge-Thierry et al. (2001)*. Here we employ extension suggested recently by *Gallovič and Brokešová (2004)*. Basic features of the model used in this study (as well as in the paper by *Gallovič and Brokešová, 2004)* are namely: 1) non-constant slip distribution, 2) variable shape of the slip rate function over the fault, 3) constant rupture velocity, 4) source spectra satisfying ω^2 scaling law, 5) high frequency randomness and complexity of the waveforms.

The rupture model involves a number of free parameters (fault dimensions, slip roughness, maximum rise time, slip velocity function), thus providing a flexible tool for simulating a variety of earthquakes. Up to now, the sensitivity of spatial distribution of acceleration (PGA maps) on the individual parameters has not been studied in detail. The goal of this paper is such a parametric study. We use the 1999 Athens earthquake of $M_w = 5.9$ as a test example.

2. METHOD

The 1D slip distribution along a line fault is characterized *(Bernard and Herrero, 1994*) by the asymptotic spectral decay k^{-2} beyond corner wave number $k_c = 1/L$, where L is the characteristic dimension of the fault (length). Up to the corner wave number the slip spectrum does not depend on k. The 2D slip distribution $D(\boldsymbol{k})$, where $\boldsymbol{k} = (k_x, k_z)$, for a rectangular fault of length L and width W can be described by its spatial Fourier spectrum:

$$D(k_x,k_z) = \frac{\Delta\bar{u}LW}{\sqrt{1+\left(\left(\frac{k_xL}{K}\right)^2+\left(\frac{k_zW}{K}\right)^2\right)}}\mathrm{e}^{\mathrm{i}\Phi(k_x,k_z)}, \tag{1}$$

where $\Delta\bar{u}$ denotes the mean slip and K is an optional parameter allowing to consider generalized corner wave numbers K/L and K/W. The phase spectrum Φ is considered random at any wave number, except for circle $k^2 \le (1/L)^2 + (1/W)^2$, for which the phase is chosen in such a way to obtain the final slip concentrated in the centre of the fault.

The slip distribution is generated in the following way. Random numbers are distributed in spatial domain on the discretised fault. This function (2D discrete random signal) is transformed to the wave number Fourier spectrum. The amplitudes of the spectrum are substituted by the amplitude term in (1). The phases inside the circle $k^2 \le (1/L)^2 + (1/W)^2$ are changed to get the centre of the whole dislocation in the centre of the fault $\left(\Phi(k_x,k_z) = -2\pi(k_xL/2 + k_zW/2)\right)$. The other phases (which are still random) retain. The spectrum is then transformed back to the spatial domain. This procedure can return negative values of the slip in certain locations of the fault. Such undesirable negative values are replaced by zeros. Finally, the slip is tapered on the edges

of the fault by a double cosine spatial window and the distribution is normalized to conserve the given seismic moment.

The *K*-parameter characterizes the slip roughness (see several illustrative examples in Fig. 1). The larger/smaller *K* is, the more/less dramatic slip variation over the fault we obtain. More specifically, provided that we assume constant mean slip and we increase *K*, we can observe that the maximum value (and consequently the gradient of the slip distribution) increases as well. As regards the slip gradient, it is linked to the stress drop distribution, and the stress drop is linked to the height of the acceleration plateau. Thus, the larger *K* is, the larger amplitudes of the radiated acceleration pulses are generated. *Gallovič and Brokešová (2004)* concluded from indirect observations that *K* value should be around 1. In this paper we vary this parameter in order to study its effect on the radiated wave field numerically. To be able to observe the possible trend clearly, the *K* value is varied in larger range around 1.

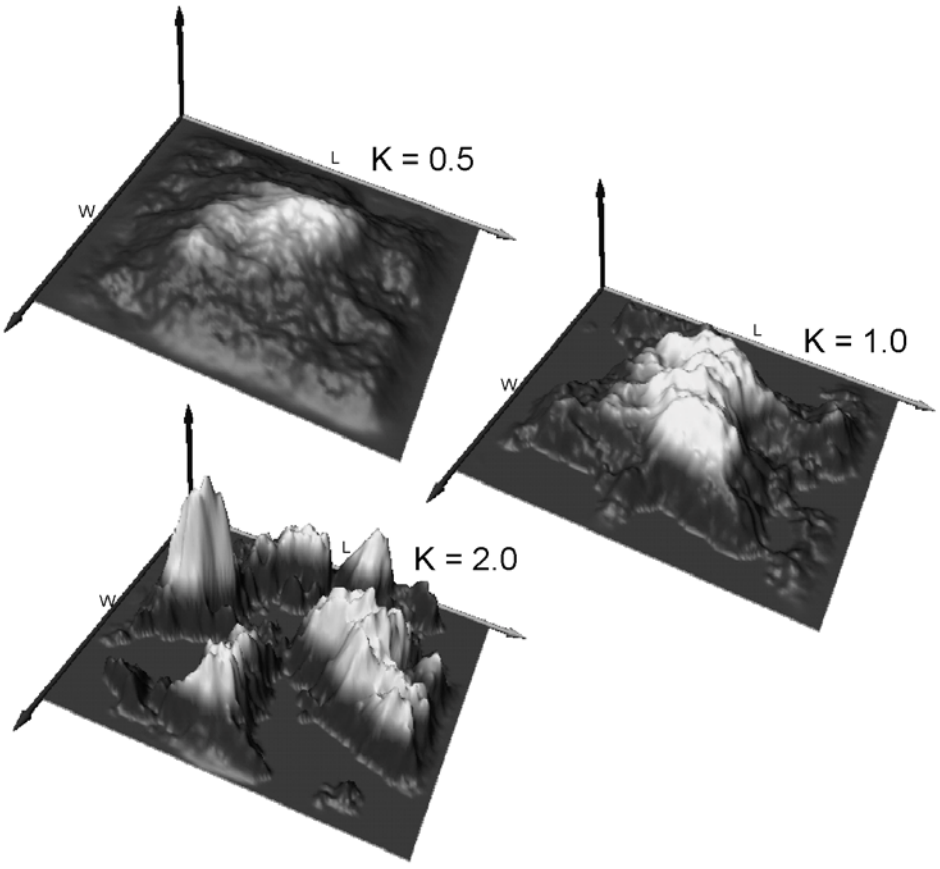

Fig. 1. Three k^{-2} slip distributions for different values of *K* - the parameter controlling the corner wave number in (1). The mean slip is the same for all these cases.

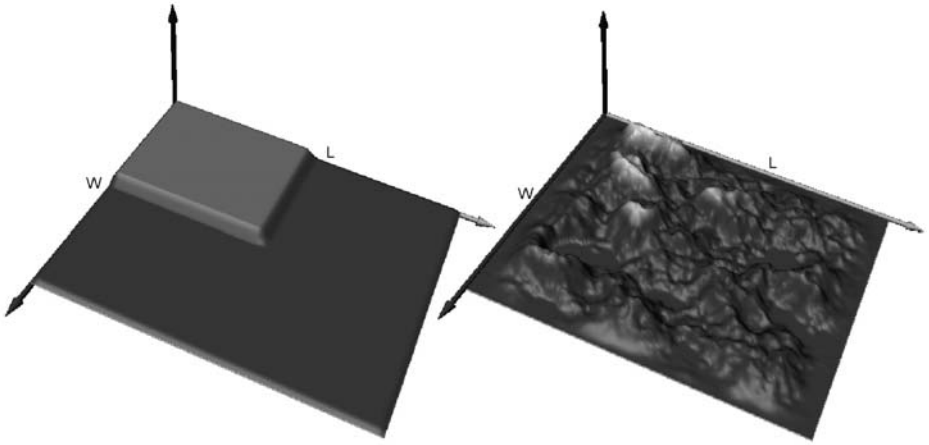

Fig. 2. An example of the hybrid slip model with an asperity covering 1/4 of the fault area. Left: the deterministic part of the slip distribution. Right: the hybrid slip combining the deterministic and stochastic (k^{-2} with $K = 1$) parts while preserving the mean slip. (Note that this mean slip is different than the one used in Fig. 1).

Note that $K = 1$ means one slip patch over the whole fault (see Fig. 1). However, for moderate to large magnitudes, in general, the slip inversions (see http://www.seismo.ethz.ch/staff/martin/research/srcmod/srcmod.html for database of available inverted slip models) indicate occurrence of two or more asperities on the fault at various positions. Thus, in order to generate slip models consisting of asperities, but with K around 1 retaining the k^{-2} spectral decay at high wave numbers, Gallovič and Brokešová (2004) suggested the hybrid slip model. It can be obtained in the following way. We consider the deterministic part of the final slip on long scales (Fig. 2 left) and then the stochastic part of the slip is superimposed on the remaining scales (Fig. 2 right). By superimposing we mean that at high wave numbers (above wave number equal to reciprocal of the size of the smallest asperity) the spatial spectrum of the deterministic part is replaced by expression (1), in which Φ is random.

Gallovič and Brokešová (2004) showed that any slip velocity function with k-dependent rise time τ with asymptotic decay k^{-1} (introduced by *Bernard et al., 1996*, for 1D fault) and k^{-2} slip distribution provides acceleration spectra satisfying ω^2 scaling law. In such model, the rupture propagates at constant velocity v in form of a slip pulse of width L_0 (connected with maximum rise time $\tau_{\max} = L_0/v$). Slip inhomogeneities of shorter characteristic dimensions than L_0 rupture in time proportional to their spatial wavelength. For 2D rectangular fault, *Gallovič and Brokešová (2004)* proposed k^{-1} dependence of the rise time in the following radially symmetric form:

$$\tau(\boldsymbol{k}) = \frac{\tau_{\max}}{\sqrt{1+\left(\frac{L_0 k}{a}\right)^2}}, \quad k = |\boldsymbol{k}|, \tag{2}$$

where a is a non-dimensional coefficient which controls, for given slip wavelength λ ($\lambda = 1/k$), the ratio of the rise time to the time necessary for the rupture front to cover the distance λ. We consider $a = 0.5$ (suggested by *Bernard et al., 1996*).

In our parametric study we use L_0 instead of $\tau_{\max}$ as one of the tested parameters. The quantity L_0 is more suitable because it can be easily related to fault dimensions.

Gallovič and Brokešová (2004) proposed an analytical expression for the strong motion synthesis based on the representation theorem (see, e.g., *Aki and Richards, 1980*) taking into account the k-dependent rise time. Acceleration spectrum $\ddot{\boldsymbol{u}}$ corresponding to a receiver at position $\boldsymbol{r}$ can be computed according to the following formula:

$$\ddot{\boldsymbol{u}}(\boldsymbol{r}, f) = \iint_{\Sigma} d\boldsymbol{\xi}\, \dot{\boldsymbol{H}}(\boldsymbol{r}, f; \boldsymbol{\xi})\, \mathrm{e}^{-2\pi \mathrm{i} f t_r(\boldsymbol{\xi})} \Delta\dot{u}(\boldsymbol{\xi}, f) \tag{3}$$

with $\Delta\dot{u}(\boldsymbol{\xi}, f)$ being the inverse spatial Fourier transform of slip velocity function.

$$\Delta\dot{u}(\boldsymbol{\xi}, f) = \iint d\boldsymbol{k}\, D(\boldsymbol{k})\, X\left(f\tau(\boldsymbol{k})\right) \mathrm{e}^{2\pi \mathrm{i} \boldsymbol{k}\cdot\boldsymbol{\xi}}\,, \tag{4}$$

where $\boldsymbol{\xi}$ denotes the position on the fault, $D(\boldsymbol{k})$ is the final slip for a given wave number (see Eq.(1)), $X(f)$ is the Fourier transform of slip velocity function of 1sec duration corresponding to unit final slip, t_r is the rupture time and $\boldsymbol{H}$ is the impulse response of a medium (dot above the letter indicates time derivative). Note that the product $f\tau(\boldsymbol{k})$ (argument of X in Eq.(4)) comes from time scaling of the slip velocity function to appropriate rise time $\tau(\boldsymbol{k})$ in time domain.

3. THE 1999 ATHENS EARTHQUAKE - BASIC INFORMATION

The Athens earthquake occurred in the area of Attica on September 7, 1999 at 11:56:50 GMT (*Papadopoulos et al., 2000*). It surprised seismologists with its $M_w = 5.9$ since there was no evidence (historical records, instrumental data) supporting events with magnitude $M_w > 5$ at distances smaller than 30 km from Athens. Maximum intensity (XIII–IX) was found in the NW outskirts of Athens. In the area, the earthquake took the toll of 143 victims and injured more than 2,000 people.

The location and focal mechanism have been determined by a number of seismological agencies (National Observatory of Athens - NOA, U.S. Geological Survey – USGS-NEIC, Harvard, Geophysical Laboratory of the Thessaloniki University and others). The locations of the epicentre are in the range of 38.02°–38.15°N and 23.55°–23.71°E. In this paper, we consider the epicentre location given by NOA after relocation: 38.08°N and 23.58°E (see Fig. 3).

The source depth, determined by the above mentioned agencies, varies from 9 to 30 km. Here we use 12 km (*Zahradník, 2002*) constrained by the amplitude spectra of complete regional seismograms.

The focal mechanisms, determined by various agencies, seem to be quite consistent (for review see *Tselentis and Zahradník, 2000a*). We consider the solution given by USGS-NEIC: strike 123°, dip 55° and rake −84°. The main shock fault plane was chosen

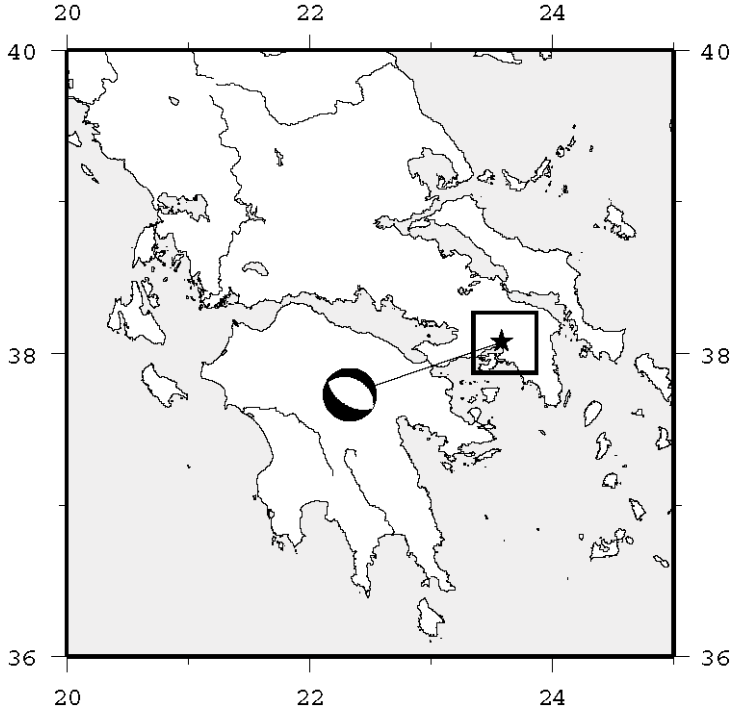

Fig. 3. NOA epicentre location (star) of the 1999 Athens earthquake and its focal mechanism (USGS-NEIC) on the map of Greece. The area of interest is indicated by a rectangle.

(from the two nodal planes) by recognizing the aftershock spatial clustering using a 30-station temporal network of the University of Patras (*Tselentis and Zahradník, 2000b*).

Plicka and Zahradník (2002) inverted regional data from 7 broadband stations in Greece by the Empirical Green's Function (EGF) method to obtain the position of the rupture area with respect to the fixed hypocentre position. They found the nucleation point on the western edge of the fault. Thus, the rupture propagated mainly in the strike direction, towards Athens. It resulted in directivity effect confirmed by: 1) teleseismic data (*Sargeant et al., 2000*), 2) shapes of apparent source time functions obtained by *Baumont et al. (2002)* from regional data, 3) short apparent time functions (about 3 sec) of strong-motion accelerograms in Athens (*Tselentis and Zahradník, 2000a*), 4) macroseismic data (intensities and corresponding PGA's according to Table 1, see Fig. 4), published by NOA.

4. FAULT DIMENSIONS

Since the rupture process of the Athens earthquake occurred on a buried fault, no direct measurements of the fault dimensions can be made. The following items review the estimates provided by various studies:

Table 1. The empirical relation between the macroseismic intensity and PGA. After *Willmore (1979)*.

Intensity	a (cm/s^2)
V	12 – 25
VI	25 – 50
VII	50 – 100
VIII	100 – 200
IX	200 – 400
X	400 – 800

- The study of teleseismic recordings by *Louvari and Kiratzi (2001)* suggests the fault dimension 18 × 10 km^2.
- The fault dimension 7.5 × 6 km^2 was found plausible by *Zahradník and Tselentis (2002)* to generate reasonable PGA's (see Fig. 5). The authors used a hybrid method (so-called PEXT method), which is based on deterministic modelling of generated wave-field up to a frequency a little higher than the corner frequency. The flat part of the acceleration spectrum behind the corner frequency is extrapolated by a spectrum of a stochastic white noise to satisfy ω^2 model and to

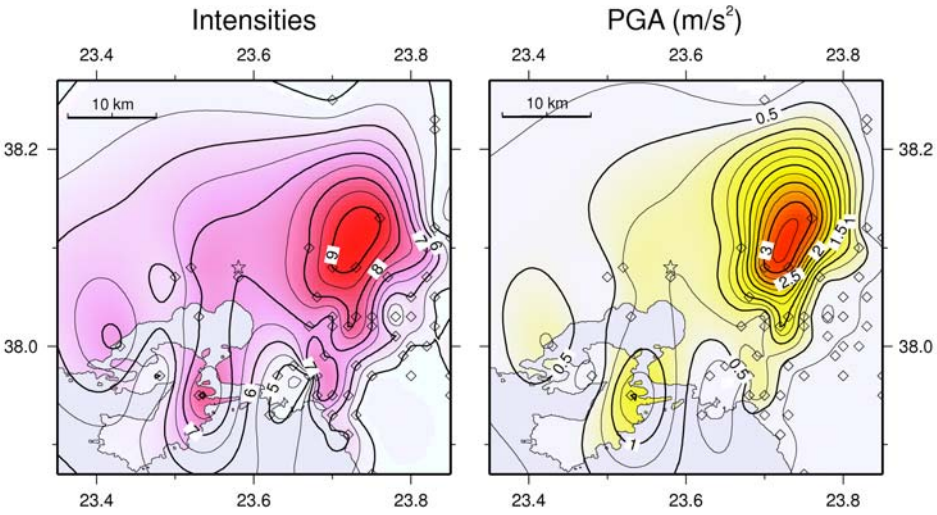

Fig. 4. Observed intensities I (left), published by NOA, and PGA map (right) computed according to mean values in Table 1. The maps were obtained by interpolating the values from data points represented by diamonds. The star denotes the NOA epicentre.

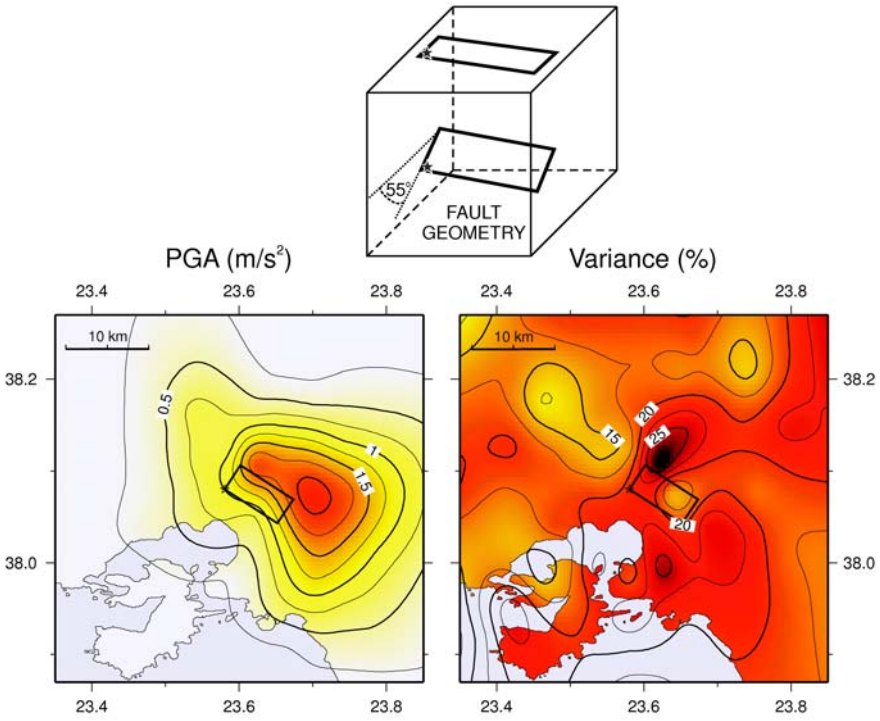

Fig. 5. PEXT simulation of the Athens earthquake with 7.5×6 km^2 fault under the assumption of homogeneous slip. The rectangle represents the projection of the fault on the earth's surface, the star represents the NOA epicentre. Normal distribution of PGA is assumed and the variance is calculated as relative standard deviation. Modified after *Zahradník and Tselentis (2002)*. The scheme of fault geometry is drawn above the maps.

preserve the duration of the deterministic part. In the deterministic part of the method, the composite modelling with equally sized subevents and spatially constant slip is used.

- The spatial distribution of aftershocks suggests two possible dimensions of fault (*Tselentis and Zahradník, 2000a,b*, see Fig. 6): 20×16 km^2 with the assumption that the strain on the fault was not fully released during the mainshock and the remaining strain was released by aftershocks; 8×10 km^2 with the assumption that the main shock released complete strain and the aftershocks occurred in the surroundings. The EGF modelling of regional data by *Plicka and Zahradník (2002)* was not able to resolve the dimension of the fault between 20×16 km^2 and 8×10 km^2. It should be noted that the network started to operate 7 days after the main shock. This suggests that the mainshock fault could have been somehow smaller than 8×10 km^2, e.g., the above mentioned 7.5×6 km^2 or even smaller. That is why we start our parametric study with 5×4 km^2 fault model.

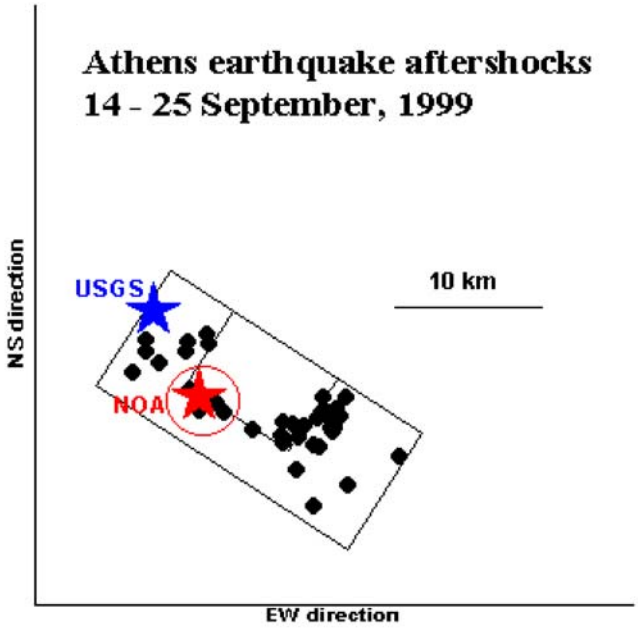

Fig. 6. The map view of September 1425, 1999, aftershocks (full circles) and two alternative faults, 8×10 km^2 and 20×16 km^2, proposed by *Tselentis and Zahradník (2000a,b)*. The USGS-NEIC and NOA (relocated) epicentres are denoted by stars (after *Plicka and Zahradník, 2002*).

- Another possibility is to utilize some empirical relations to estimate fault dimensions for the magnitude. For example, *Somerville et al. (1999)* estimate the area of the fault $A = 88$ km^2. *Mai and Beroza (2000)* suggest 12×9 km^2.

Since the question of fault dimensions is still open, we try to test some of the above suggested values, together with the other source parameters.

5. COMPUTATIONAL DETAILS

We consider the crustal model, used for discrete wave number modelling of regional data by *Tselentis and Zahradník (2000a)*. This 1D structural model consists of homogeneous layers listed in Table 2. The uppermost 1 km low-velocity layer is partly confirmed by the surface waves dispersion study by *Novotný et al. (2001)*.

The parameters of the Athens earthquake we keep fixed in our study are listed in Table 3. We assume that the nucleation point is located in the bottom left (western) corner of the fault at 12 km depth. The rupture propagates radially at constant rupture velocity v. We assume the ratio of rupture to *S*-wave velocity (in the vicinity of the fault) to be approximately 0.8, i.e. $v = 2.8$ km/s.

Table 2. Parameters of the crustal model used.

Bottom Depth [km]	v_p [km/s]	v_s [km/s]	ρ [g/cm^3]
1	2.67	1.50	2.50
2	4.45	2.50	2.50
5	5.70	3.20	2.84
18	6.00	3.37	2.90
39	6.40	3.60	2.98
halfspace	7.90	4.44	3.28

Table 3. Fixed parameters for the Athens earthquake model.

Epicentral latitude (N)	36.08°
Epicentral longitude (E)	23.58°
Hypocentral depth [km]	12.00
Seismic moment [Nm]	7.8×10^{17}
Strike	123°
Dip	55°
Rake	–84°
Rupture velocity [km/s]	2.8

High frequency accelerograms have been computed using the standard zero-order ray theory (far-field approximation). In this study we restrict ourselves to the epicentral region < 50 km, in which the surface waves are not assumed to be significant (due to the source depth). We consider that the direct *S* wave represents the most important part of the wave field in terms of acceleration amplitudes for our particular source and structural model, so that only direct *S* waves are taken into account. This assumption has been confirmed by many authors (e.g., *Hanks, 1982*; *Berge-Thierry et al., 2001*; *Zollo et al., 1997*; *Emolo and Zollo, 2001*; *Gasperini, 2001*, etc.).

The computer code for 2D ray computations BEAM87 written by V. Červený and modified by *Brokešová (1993)* to allow for 2.5D computations is used. Under the 2.5D computation we understand computation of 3D rays in 2D medium (i.e. medium with properties dependent on vertical and one horizontal coordinate). However, when calculating rays in our particular (1D) model, we do not take the full advantage of this approach.

The kinematic modelling requires a relatively large number of point sources distributed over the fault to avoid artificial numerical effects (such as spatial aliasing) when evaluating numerically the representation integral. To decrease numerical costs, interpolation is desirable. The zero-order ray solutions are determined by three parameters for each ray: the arrival time and the real and imaginary parts of the amplitude. Only these quantities have to be interpolated. Moreover, the changes of these parameters with respect to the position on the fault have been found smooth in our particular crustal model. It allows for using bicubic splines (which are suitable for their smoothness) as interpolation functions.

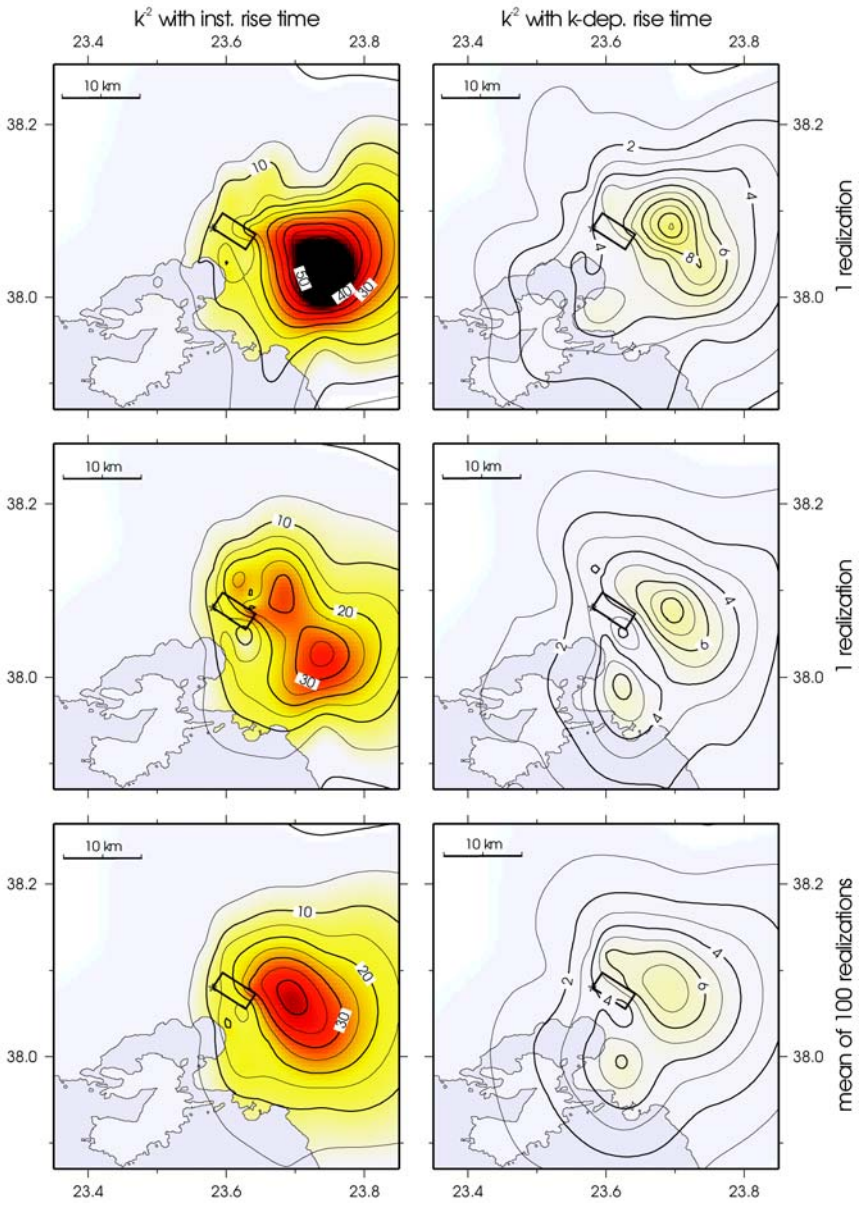

Fig. 7. PGA maps in m/s^2 for instantaneous rise time (left) and the wave number dependent rise time (right) for the fault dimensions 5×4 km^2 ($L_0 = 0.20L$). The figure shows results for two different realizations of the slip distribution (top and middle) and the mean result of 100 realizations (bottom). The rectangles represent the projection of the fault to the earth's surface. The star denotes the epicentre.

For simplicity, in this parametric study we consider the frequency range up to 5 Hz. The spatial sampling of the fault is at least 100 m, which corresponds to about 6 samples per wavelength at the source. The attenuation effects are neglected. Site effects are not taken into account, thus, from this point of view our results would correspond rather to low-pass filtered seismograms on bedrock.

To produce the maps of PGA values in the vicinity of the fault, the receivers are distributed on 16 radial line profiles, intersecting at epicentre, with azimuthal increment of 22.5°. On each profile there are 5 receivers at the epicentral distances of 5–25 km with step of 5 km. The horizontal PGA's computed at these receivers are used to generate PGA maps by interpolation. Under the horizontal PGA we understand the magnitude of the vectorial sum of both horizontal time history components.

6. 5×4 km^2 FAULT MODEL

We start with fault dimensions somewhat smaller than 8×10 km^2 found from the aftershock distribution: we choose 5×4 km^2. We assume $K = 1$.

Fig. 7 shows PGA maps generated by k^{-2} rupture model with either instantaneous rise time (i.e. δ-function represented by $X(f) = 1$ in Eq.(4)) or wave number dependent rise time ($L_0 = 0.20L$, boxcar slip velocity function) for two different realizations of final slip on the fault. The bottom part of the figure shows the mean PGA map of 100 realizations (normal distribution of PGA's is assumed). The map of variance (relative standard deviation of normal distribution in percents) for the case of k-dependent rise time is on the right in Fig. 8. The variance is about 20–30% everywhere and does not exhibit any systematic behaviour with respect to the position of the fault.

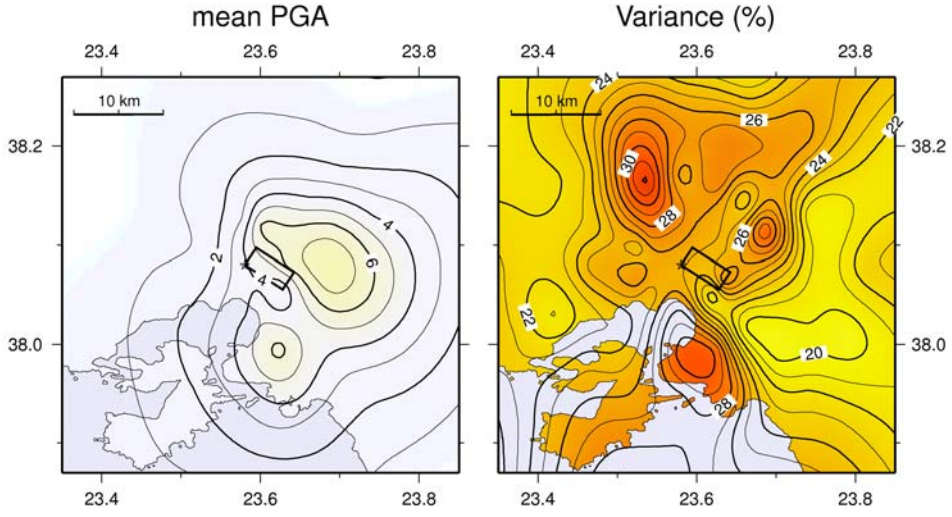

Fig. 8. The mean PGA map in m/s^2 (the same as in the right bottom of Fig. 7) for wave number dependent rise time (left) and the map of its variance (right).

In Fig. 7 we can see that the area of highest PGA is located eastward from the epicentre in all cases. It is a consequence of the combination of two effects: directivity and *S* wave radiation pattern. To enlighten the latter, Fig. 9 shows how the PGA map changes when the double couple radiation pattern (Fig. 10) is neglected (isotropic radiation from each point source is considered). Without the radiation pattern, the maximum is basically in the strike direction due to the directivity effect. In that direction, however, the radiation pattern has its minimum. As a consequence, the radiation pattern shifts the area of maximum PGA values on the map a little to the north.

Let us discuss the overall appearance of the PGA maps. The presented maps (top and middle in Fig. 7) are the representatives of two different types of PGA maps which we have obtained for this model. In the top, the maps have the PGA maximum focused around one point on the surface while, in the middle, the maps have the PGA maximum split into two spots. Considering *k*-dependent rise time instead of instantaneous one changes a bit the shape and position of the high PGA area but the map qualitatively remains similar.

As it can be seen in Fig. 7, the PGA values predicted by the model with instantaneous rise time are more than 5 times higher than those simulated by the model with wave number dependent rise time. Moreover, the PGA map for the instantaneous rise time shows more than 40 times higher values in the direction of the rupture propagation than in the opposite direction. Such a strong directivity effect was discussed for a line fault in the Fraunhoffer's approximation by *Bernard and Herrero (1994)*. This strong directivity effect has never been observed. That's why this model was revised by *Bernard et al. (1996)* and the *k*-dependent rise time was introduced.

On the other hand, the k^{-2} rupture model with instantaneous rise time was successfully used for strong motion prediction by, e.g., *Zollo et al. (1997)* and *Emolo and Zollo (2001)*. They predicted reasonable mean PGA values because they compute the means from

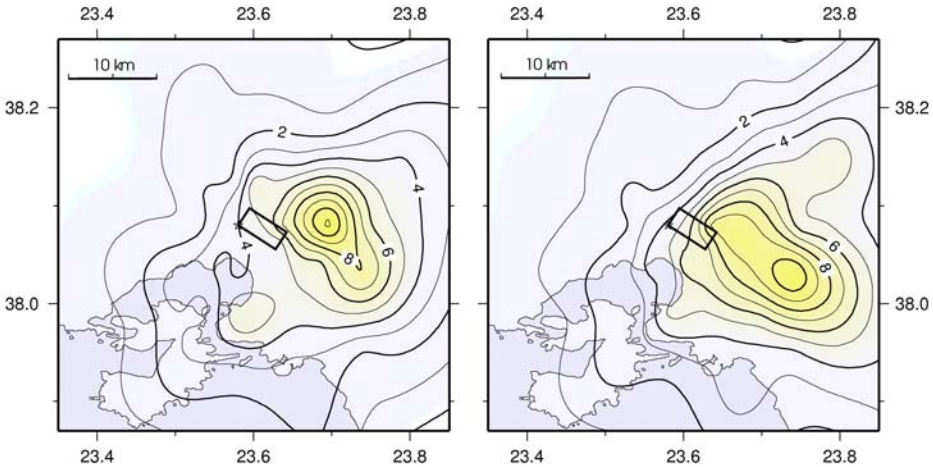

Fig. 9. The influence of the *S* wave radiation pattern (see Fig. 10) on the PGA maps: the radiation pattern is taken into account (left, the same as in Fig. 7 top right) and it is neglected (right). The right map is scaled by the largest value of PGA in the left figure.

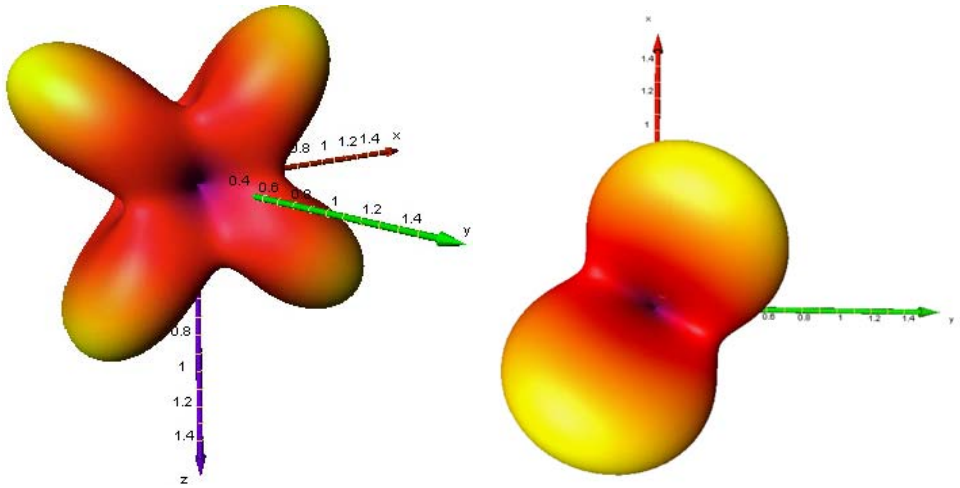

Fig. 10. The figures show the used *S* wave radiation pattern (square root of the sum of SH and SV radiation patterns squared) in two different view angles. The *x*-axis goes to the north, the *y*-axis to the east.

results obtained with nucleation point position varying on the fault. Note that if we put the nucleation point on the opposite side of the fault (bottom right), the area of highest PGA would move to the opposite side with respect to the fault. The mean values would then be much lower, hence providing "realistic" estimates.

Although the *k*-dependent rise time gives lower PGA values than the instantaneous, it is obvious that they are still overestimated. In the following we investigate whether considering a different slip velocity function can make any difference.

Results for different combinations of two widths of the slip pulse ($L_0 = 0.20L$ and $L_0 = 0.05L$) and three types of slip velocity functions (boxcar, Brune's and Hisada's, see Fig. 11) are shown in Fig. 12. The slip distribution is considered the same as for the first realization in Fig. 7.

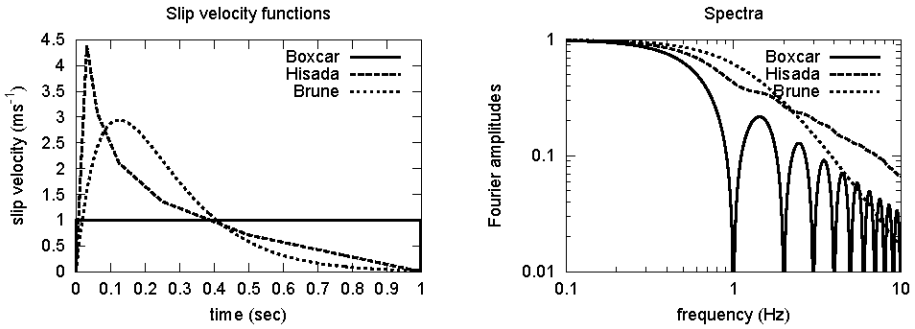

Fig. 11. Three slip velocity functions (left) used in this study with their amplitude spectra (right). Hisada's and Brune's functions are constructed according to *Hisada (2000)* and *Brune (1970)*, respectively. All three functions have 1 sec duration and correspond to unit final dislocation.

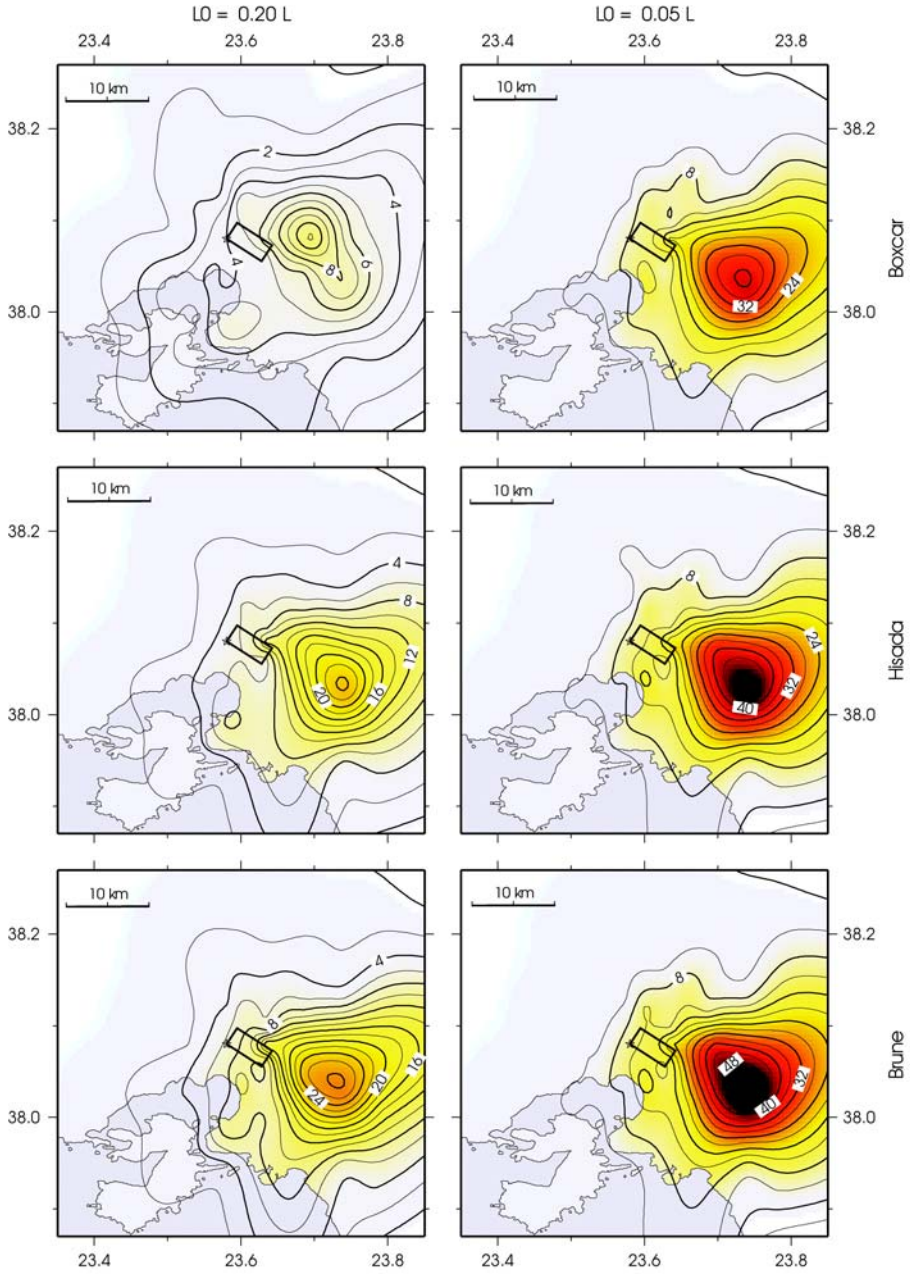

Fig. 12. PGA maps in m/s^2 for two slip pulse widths (0.20*L* and 0.05*L*) and three slip velocity functions. The slip distribution is the same as was used for the maps in the top of Fig. 7. The position and the size of the fault is the same as in Fig. 7.

Qualitatively, the shape of the maps remains the same as in Fig. 7. We can see that in the broad pulse case (left part of the figure) the use of the boxcar slip velocity function results in the lowest estimates of PGA when compared to the results for the other two functions. This phenomenon is not so pronounced for the narrow pulse. In this case, the values nearly reach those for the instantaneous rise time. That is why we prefer the broad pulse. The effect of narrowing the slip pulse on the PGA maps is displayed in more detail (four values of L_0) in Fig. 13 where only the Hisada's slip velocity function is considered.

The maps obtained for instantaneous and boxcar slip velocity functions represent, in general, two extremes in terms of maximum PGA from the set of all slip velocity functions considered. It is because instantaneous and boxcar functions are extremes from the point of view of maximum slip velocity among all other possible slip velocity functions corresponding to the same final slip.

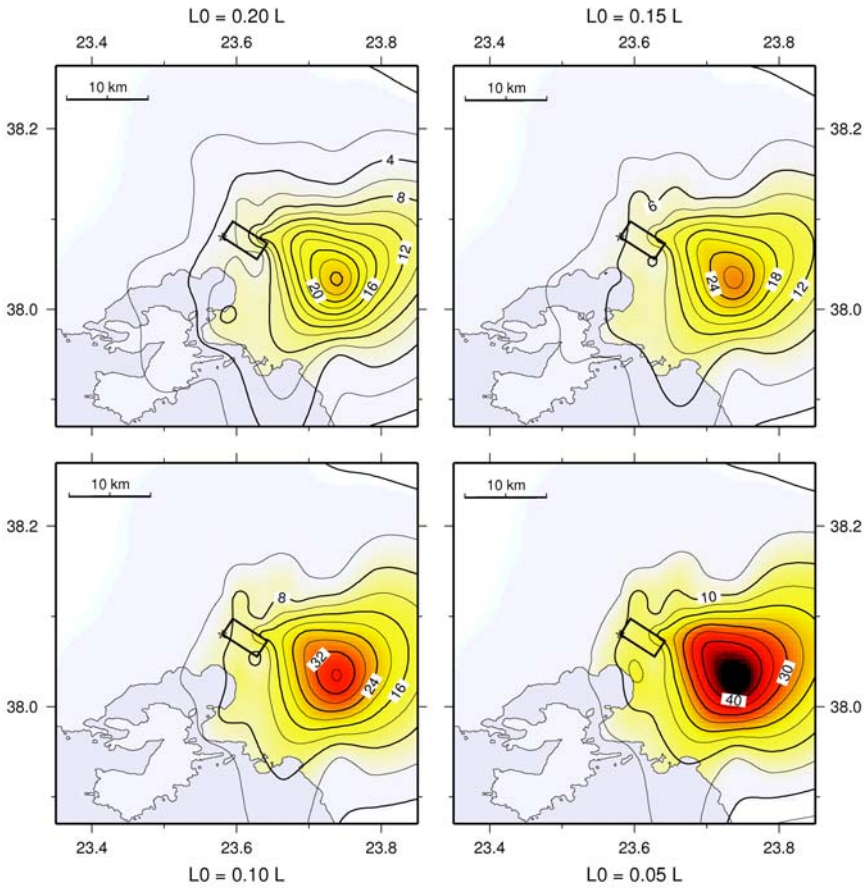

Fig. 13. PGA maps in m/s^2 illustrating the influence of various pulse widths from $L_0 = 0.05L$ to $L_0 = 0.20L$. The slip distribution is the same as it was used in Fig. 12. The Hisada's slip velocity function is used. The position and the size of the fault is the same as in Fig. 7.

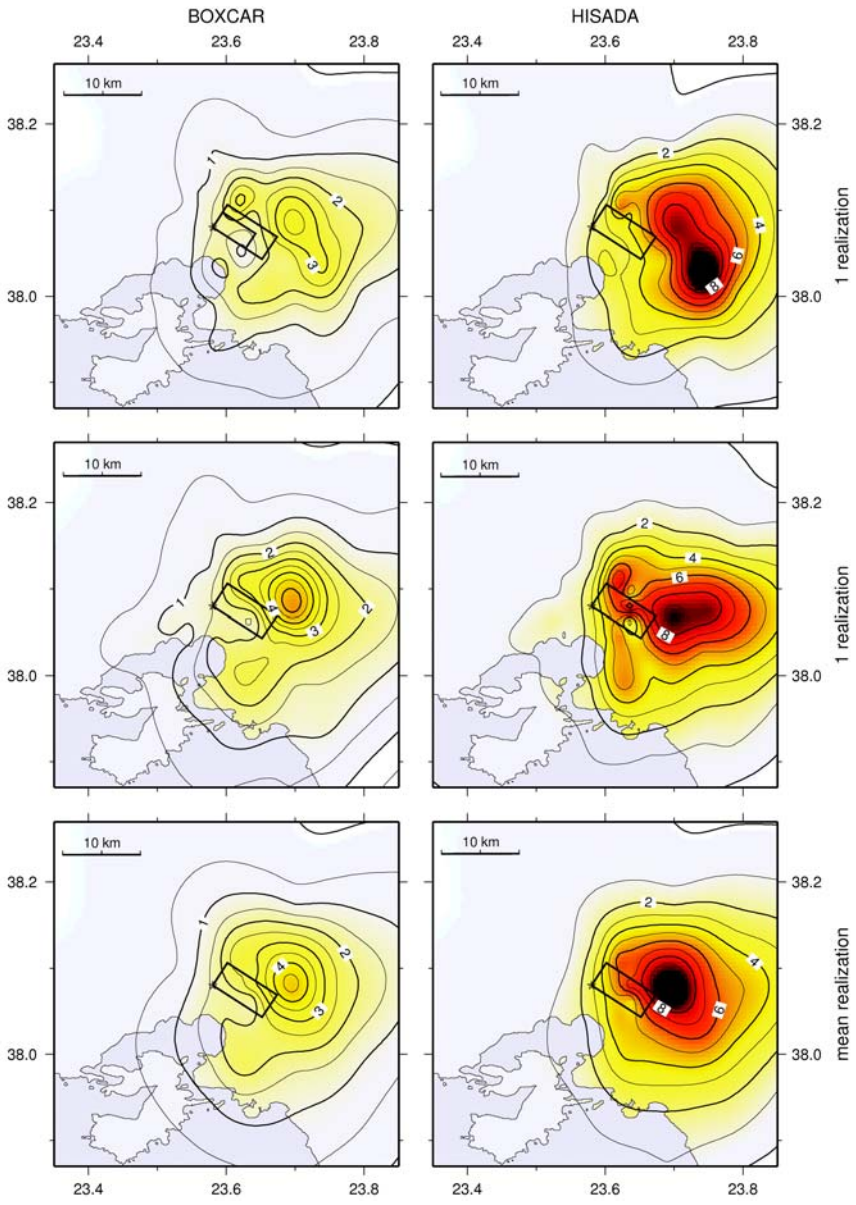

Fig. 14. PGA maps in m/s^2 for 7.5×6 km^2 fault model and two slip velocity functions ($L_0 = 0.20L$ in both cases). In the top and the middle part the figure shows results for two different realizations of the slip distribution. The mean result of 100 realizations is shown in the bottom. For comparison, the 5×4 km^2 fault studied before is displayed on the top left map. The star denotes the epicentre.

All our above mentioned PGA maps indicate that the PGA's are still overestimated, which is the consequence of relatively small fault dimensions (i.e. relatively large mean slip) for the given seismic moment. This leads us to consider a larger fault.

7. 7.5 × 6 km^2 FAULT MODEL

Here we assume the fault of dimension 7.5 × 6 km^2 (corresponding to result of *Zahradník and Tselentis, 2002*). Hisada's and boxcar slip velocity functions and $L_0 = 0.20L$ are used to generate PGA maps in Fig. 14 for two different realizations of slip distribution. Fig. 14 shows also the mean PGA map for 100 slip realizations. The map of variances is not displayed because it does not exhibit any systematic behaviour similarly to the previous case. The variances are about 25–35%.

The maps in the bottom of Fig. 14 seems to be quantitatively similar to those in Fig. 12. The simulations with the Hisada's slip velocity function give about twice higher values of PGA than those corresponding to the boxcar function. Nevertheless, the shape of the maps, which is caused mainly by the directivity and the *S* wave radiation pattern, is very similar to each other. As expected, the simulated PGA values are much lower than those for the smaller 5 × 4 km^2 fault because the mean slip decreases when increasing the fault dimensions (while seismic moment is kept constant).

The 7.5 × 6 km^2 fault was found plausible by the PEXT simulation by *Zahradník and Tselentis (2002)*. However, in the PEXT method a constant slip was assumed. Our heterogeneous slip results in higher PGA estimates (compare with Fig. 5).

The *K*-parameter involved in our slip model allows to vary the smoothness of the slip distribution. By considering $K < 1$ we achieve a smoother slip (see Fig. 1). The PGA maps for $K = 0.5$, $K = 1.0$ and $K = 2.0$ ($L_0 = 0.20L$) are displayed in Fig. 15. The figure testify that the higher *K* is (and, consequently, the higher maximum slip values and the slip gradient are), the higher PGA's we obtain (see also the explanation in Section 2.).

The PGA values for $K = 0.5$ are still relatively high but it is obvious that we would have similar results as PEXT by decreasing *K*. However, the slip would be perhaps too smooth. To avoid this, one possibility is to extend the fault dimensions and keep *K* between 0.5 and 1.0, or to assume an asperity model of the rupture. The presence of asperities is a common feature of the slip inversion results.

8. ASPERITY MODEL

We choose two examples from a large set of possible asperity models. We extend the widths and the lengths of the above considered faults twice in down-dip and along-strike directions, respectively. In this way we obtain the models where the asperity covers 1/4 of the fault area (which is based on empirical relations by *Somerville et al., 1999*). This results in the "smaller" fault 10 × 8 km^2 and the "larger" fault 15 × 12 km^2 with an asperity 5 × 4 km^2 and 7.5 × 6 km^2, respectively.

To model the slip distribution with an asperity, we take the advantage of our ability to combine the deterministic part of slip (asperity in our case) at low wave numbers and the stochastic k^{-2} distribution for the higher ones.

Another free parameter occurs in asperity models: the ratio of the mean slip on the asperity and the mean slip over the whole fault, the so-called slip contrast. We choose two slip contrast values: 2 and 3.

The mean PGA maps for four cases (two fault dimensions and two slip contrasts) are displayed in Fig. 16. The width of the slip pulse is chosen to correspond to 20% of the asperity length L_a, thus, 10% of the fault entire length L, i.e. $L_0 = 0.20L_a = 0.10L$. As an example, two synthetic seismograms (and their spectra) obtained at two stations located at the same epicentral distances (10 km) but at different azimuths are shown in Fig. 17. The first one lies in the direction of rupture propagation while the second one is situated in the backward direction. As we can see, station lying in the direction of rupture propagation exhibits shorter duration and larger amplitudes of the record with respect to records at the station in the opposite direction. Concerning their synthetic amplitude spectra, we can

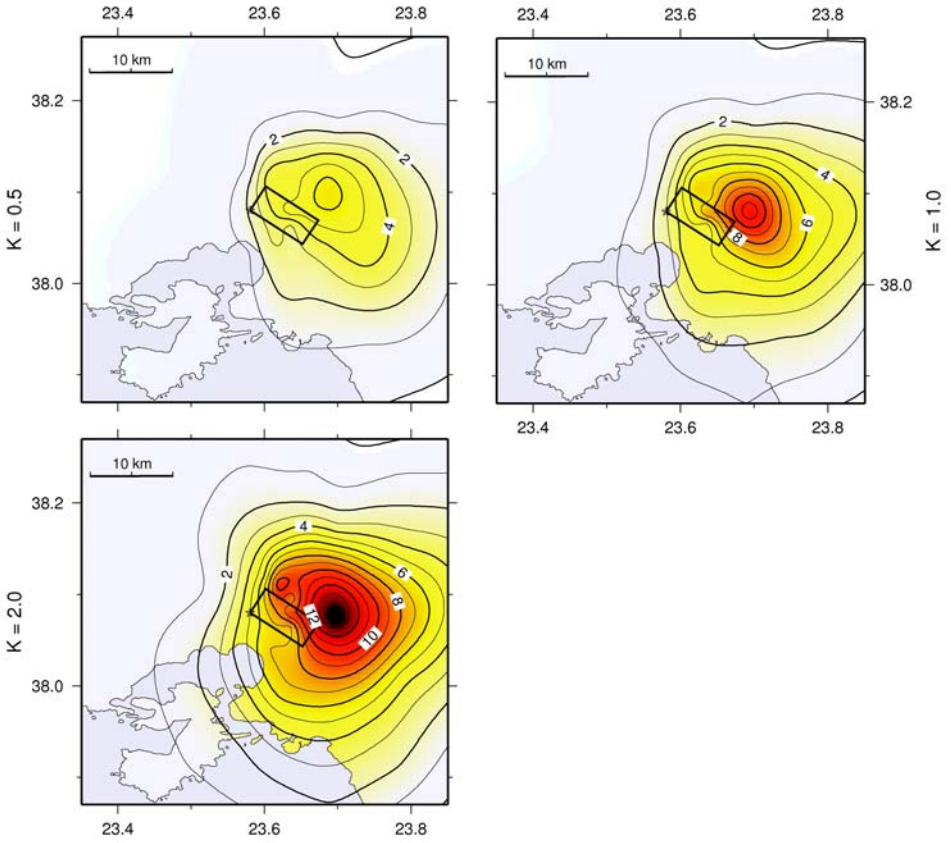

Fig. 15. PGA maps in m/s^2 for 7.5 × 6 km^2 fault model with fixed $L_0 = 0.20L$ and varying K. The Hisada's slip velocity function is used. The position and the size of the fault is the same as in Fig. 14.

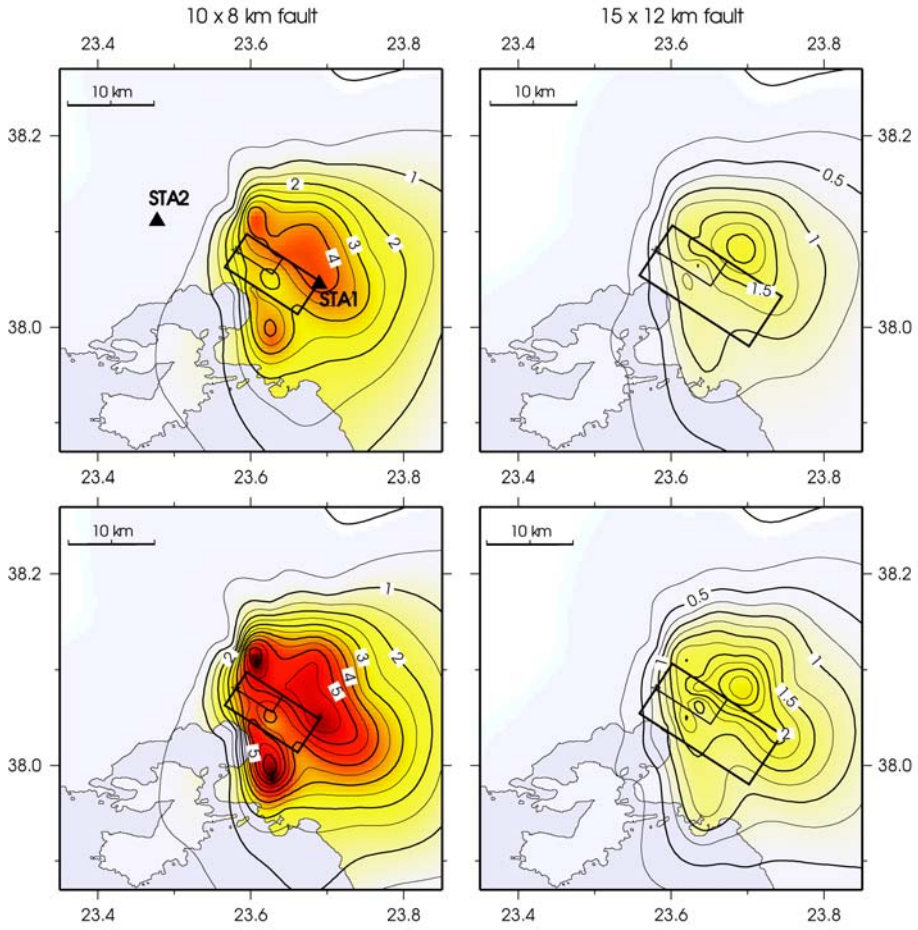

Fig. 16. Maps of PGA means (in m/s^2) over 100 realizations for various asperity models. In each model we consider that the asperity covers 1/4 of the fault. Two sizes of the entire fault (left, right) and two slip contrasts 2 (top) and 3 (bottom) are shown. The rectangles in the middle of each map represent the projections of the fault and the asperity to the earth's surface. The star denotes the epicentre. $L_0 = 0.10L$, $K = 1$, Hisada's slip velocity function is used. An example of accelerograms synthesized (for one slip realization) at stations indicated in the top left map can be found in Fig. 17.

observe that the corner frequency and the height of the spectral plateau is higher in the forward direction than in the backward direction.

We can see from Fig. 16 that the simulated PGA values are roughly comparable with the observed data (Fig. 4) in these cases. Nevertheless, it is clear that such a comparison cannot be used to verify our computation results because neither attenuation nor site effects are taken into account in our modelling.

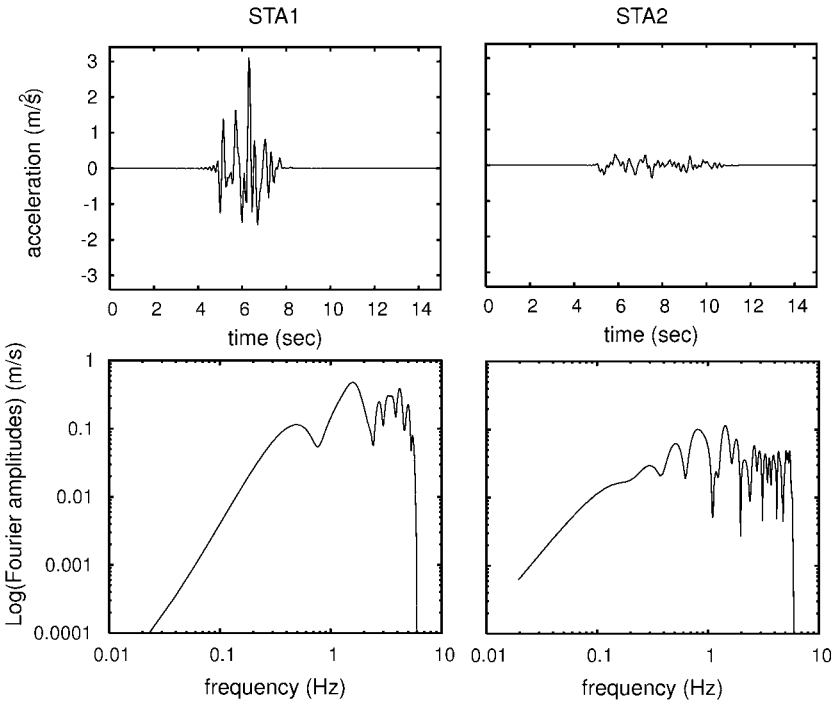

Fig. 17. Top: an example of two synthetic accelerograms (NS component) at stations indicated in top left map in Fig. 16 for the corresponding asperity model (10×8 km^2 fault with slip contrast 2, $L_0 = 0.10L$, $K = 1$, Hisada's slip velocity function). Bottom: their amplitude spectra.

9. DISCUSSION AND CONCLUSION

We have applied the k^{-2} rupture model to the 1999 Athens earthquake and have computed the PGA maps in epicentral distances < 50 km. We fixed the earthquake parameters determined by previous studies: location of the epicentre, hypocentral depth, scalar seismic moment, focal mechanism and the position of the nucleation point on the fault. Rupture velocity was set to represent 80% of the *S*-wave velocity at the nucleation point depth. The values of the remaining parameters of the k^{-2} rupture model (fault dimensions, slip pulse width, *K*-parameter and the type of the slip velocity function) were varied in this parametric study.

Usually, authors study the influence of the kinematic parameters on the radiated wave field for simple line fault in Fraunhoffer's approximation in homogeneous medium (*Joyner, 1991*; *Bernard et al., 1996*; *Gallovič and Brokešová, 2004*). Here we deal with a 2D rupture model with radial rupture propagation, so it is not straightforward to compare the results obtained in this study with that obtained for unidirectional rupture propagation along a line fault.

Due to the relative simplicity of the structural model considered in our numerical experiments, the shape of the maps is given predominantly by the directivity and the radiation pattern. Both of these effects are given by the fault geometry. The directivity effect is, moreover, affected by how rupture propagates. In our case, the rupture propagates from the nucleation point (situated in the left bottom corner of the fault) in all directions, so that it includes not only the strike direction but also the up-dip direction. Consequently, the location of the PGA spot commonly observed on our synthetic mean PGA maps (e.g., Fig. 7 bottom) cannot be easily interpreted as the manifestation of the forward directivity known from the line fault studies. Moreover, the location of the spot is strongly influenced by the radiation pattern (see Fig 9).

Let us discuss qualitative behaviour of PGA maps when changing the k^{-2} rupture parameters. The parametric study shows significant directional dependence of mean PGA's with a distinct localized maximum to the east from the epicenter. More detailed analysis of the results reveals that the directivity effect is more pronounced for the case of instantaneous rise time than in the case of the other slip velocity functions considered. We can see that the slip pulse width changes mainly the maximum PGA values, not the location of the PGA maximum. The same can be stated about K and the slip velocity functions. The fault dimensions affect both the PGA maximum values (depending mainly on the corresponding mean slip) as well as the location of the maximum on the map. However, its relative location with respect to the fault remains the same the maximum is always located close to the right edge of the fault projection to the Earth surface. The overall look of the PGA map changes significantly when an asperity on the fault is taken into account. For example, in Fig. 16 left we observe that mean PGA maximum is split into two parts. Fig. 16 also demonstrates that the PGA's are affected by both the asperity size as well the asperity slip contrast. From the calculations performed in this study it seams that the mean slip on the asperity (slip contrast) influences mainly the PGA values while retaining the shape of the maps unchanged (similarly to mean slip over the whole fault, see above).

Let us discuss the joint influence of slip pulse width and the shape of the slip velocity function on the radiated PGA. As it can be seen in Fig. 11, the Brune's and Hisada's slip velocity functions have "efficient" rise-time about one third of the one of the boxcar, or, alternatively, the Brune's and Hisada's slip velocity functions have maximum velocity about three times higher than the one of the boxcar. The details of the slip velocity history (sharp or slow increase or decrease) play only a minor role for PGA maps (compare PGA maps for boxcar with narrow pulse and, e.g., Brune's with broad pulse in Fig. 12). However, we prefer using more realistic functions (e.g., Hisada's or Brune's) than the boxcar since the boxcar provides artificial zeros in spectral domain linked to sharp edges of the function.

From the practical point of view, numerical simulations should seal with comparison with real data. Some strong motion records are available for the studied event but with insufficient azimuthal coverage: the stations lie in the city of Athens, so that they are distributed in the direction of rupture propagation only. However, the primary aim of this paper is the parametric study with the emphasis to directivity effect. Thus we prefer to compare (although roughly) our results with intensities having better azimuthal coverage. The position of synthetic PGA maximum roughly corresponds to the position of

maximum intensity. Nevertheless, we have to keep in mind that although we assume relatively complex source model, the propagation effects were simplified considerably: we take into account neither inelastic attenuation nor site effects. Consequently, the complexity of the computed PGA maps is given by the source characteristic only. Thus, in our study we show that the source effect (especially directivity) could considerably contribute to the maximum intensity position. However, since the transition from measured intensities to PGA's (see Table 1) is very uncertain, our parametric study of the rupture model cannot help us to determine the details of the model: for example, whether the rupture fault was without asperity but larger than 7.5×6 km^2 (see the teleseismic estimate by *Louvari and Kiratzi, 2001*), or whether there were more asperities on relatively large fault and so on. In this study, we prefer the asperity model based on *Somerville et al. (1999)* since the asperities commonly appear in the slip distributions obtained by the slip inversions.

Many issues remain for next studies, e.g., comparison with the observed accelerograms and empirical attenuation relations. This will need to calculate the wavefield up to higher frequencies and to consider attenuation and site effects, perhaps also variations of rupture velocity and source mechanism during the rupture propagation. It would be also important to assume variability of all parameters within their range of uncertainty (hypocenter location, rupture velocity, fault dip, strike, dip and rake, K, rise-time, fault dimensions etc.), to compute mean PGA map and its variance, and, possibly, to compare the modeling result with attenuation relations.

Acknowledgements: The authors thank to Pascal Bernard for his suggestions and comments. The authors are also very grateful to Jiří Zahradník and anonymous referees for helpful review of the paper. Some of the figures were made with Generic Mapping Tools (*Wessel and Smith, 1991*). The authors were supported by the following grants: EU project EVG1CT199900001 PRESAP and several research projects in the Czech Republic MSMT DG MSM/98113200004, GACR 205/03/1047 and GAUK 176/2000/B GEO/MFF.

References

Aki K., 1967. Scaling law of seismic spectrum. *J. Geophys. Res.*, **72**, 1217–1231.

Aki K. and Richards P.G., 1980. *Quantitative Seismology: Theory and Methods.* W.H. Freeman, San Francisco, USA.

Baumont D., Courboulex F., Scotti O., Melis N. S. and Stavrakakis G., 2002. Slip Distribution of the $M_W = 5.9$, 1999 Athens earthquake inverted from regional seismological data. *Geophys. Res. Lett.*, **29**, Art. No.1720.

Berge-Thierry C., Bernard P. and Herrero A., 2001. Simulating strong ground motion with the "k-^{2}" kinematic source model: an application to the seismic hazard in the Erzincan basin, Turkey. *J. Seismol.*, **5**, 85–100.

Bernard P. and Herrero A., 1994. Slip heterogeneity, body-wave spectra, and directivity of earthquake ruptures. *Ann. Geofis.*, **XXXVII**, 1679–1690.

Bernard P., Herrero A. and Berge C., 1996. Modeling directivity of heterogeneous earthquake ruptures. *Bull. Seismol. Soc. Amer.*, **86**, 1149–1160.

Brokešová J., 1993. *High-Frequency Ground Motions due to Extended Seismic Sources in Complex Structures*. PhD. Thesis, Charles University, Prague.

Brune J., 1970. Tectonic stress and the spectra of seismic shear waves from earthquakes. *J. Geophys. Res.*, **75**, 4997–5009.

Emolo A. and Zollo A., 2001. Accelerometric radiation simulation for the September 26, 1997 Umbria-Marche (Central Italy) main shocks. *Ann. Geofis.*, **44**, 605–617.

Gallovič F. and Brokešová J., 2004. On strong ground motion synthesis with k^{-2} slip distributions. *J. Seismol.*, **8**, 211–224.

Gasperini P., 2001. The attenuation of seismic intensity in Italy: a bilinear shape indicates the dominance of deep phases at epicentral distances longer than 45 km. *Bull. Seismol. Soc. Amer.*, **91**, 1–15.

Hanks T.C., 1982. FMAX. *Bull. Seismol. Soc. Amer.*, **72**, 1867–1879.

Herrero A. and Bernard P., 1994. A kinematic self-similar rupture process for earthquakes. *Bull. Seismol. Soc. Amer.*, **84**, 1216–1228.

Hisada Y., 2000. A theoretical omega-square model considering the spatial variation in slip and rupture velocity. *Bull. Seismol. Soc. Amer.*, **90**, 387–400.

Joyner W., 1991. Directivity for nonuniform ruptures. *Bull. Seismol. Soc. Amer.*, **81**, 1391–1395.

Louvari E. and Kiratzi A., 2001. Source parameters of the 7 September 1999 Athens (Greece) earthquake based on teleseismic data. *J. Balkan Geophys. Soc.*, **4**, 51–60.

Mai M. and Beroza C., 2000. Source scaling properties from finite-fault rupture models. *Bull. Seismol. Soc. Amer.*, **90**, 604–615.

Novotný O., Zahradník J. and Tselentis G.A., 2001. Northwestern Turkey earthquakes and the crustal structure inferred from surface waves observed in Western Greece. *Bull. Seismol. Soc. Amer.*, **91**, 875–879.

Papadopoulos G.A., Drakatos G., Papanastassiou D., Kalogeras I. and Stavrakakis G., 2000. Preliminary results about the catastrophic earthquake of 7 September 1999 in Athens, Greece. *Seism. Res. Lett.*, **71**, 318–329.

Plicka V. and Zahradník J., 2002. Inversion of rupture nucleation from regional records by egf method for unequal focal mechanisms of the mainshock and aftershock: The Athens 1999 earthquake. *Tectonophysics*, **359**, 81–95.

Sargeant S.L., Burton P.W., Douglas A. and Evans J.R., 2000. A source model for the 7th September 1999 Athens earthquake. Proceedings, European Seismological Commission (ESC), XXVII General Assembly, Lisbon, Portugal, September 10–15, 138–142.

Somerville P., Irikura K., Graves R., Sawada S., Wald D., Abrahamson N., Kagawa Y.I.T., Smith N. and Kowada A., 1999. Characterizing crustal earthquake slip models for the prediction of strong ground motion. *Seism. Res. Lett.*, **70**, 59–80.

Tselentis G.A. and Zahradník J., 2000a. The Athens earthquake of 7 September 1999. *Bull. Seismol. Soc. Amer.*, **90**, 1143–1160.

Tselentis G.A. and Zahradník J., 2000b. Aftershock monitoring of the Athens earthquake of 7 September 1999. *Seism. Res. Lett.*, **71**, 330–340.

Wessel P. and Smith W.H.F., 1991. Free software helps map and display data. *EOS Trans.*, **72**, 445–446.

Willmore P.L., 1979. *Manual of Seismological Observatory Practice.* Report SE20, World Data Center A for Solid Earth Geophysics, Boulder, Colorado, USA.

Zahradník J., 2002. *Focal Mechanism of the Athens 1999 Earthquake by ASPO Method.* Res. Report, Dept. of Geophysics, Faculty of Math. and Phys., Charles University, Prague, Czech Republic (http://seis30.karlov.mff.cuni.cz).

Zahradník J. and Tselentis G.A., 2002. Modeling strong-motion accelerograms by "PEXT" method, application to the Athens 1999 earthquake. Proceedings, European Seismological Commission (ESC), XXVIII General assembly, Genoa, Italy, September 1–6, CDROM.

Zollo A., Bobbio A., Emolo A., Herrero A. and De Natale G., 1997, Modeling of ground acceleration in the near source range: the case of 1976, Friuli earthquake (M = 6.5), Northern Italy. *J. Seismol.*, **1**, 305–319.